ADVANCES IN ATMOSPHERIC SCIENCES, VOL. 34, JUNE 2017, 685–699

• **Original Paper** •

Optimal Precursors Triggering the Kuroshio Extension State Transition Obtained by the Conditional Nonlinear Optimal Perturbation Approach

Xing ZHANG[1,2], Mu MU[3], Qiang WANG[*1,4], and Stefano PIERINI[5]

[1]*Key Laboratory of Ocean Circulation and Waves, Institute of Oceanology, Chinese Academy of Sciences, Qingdao* 266071*, China*

[2]*University of Chinese Academy of Sciences, Beijing* 100049*, China*

[3]*Institute of Atmospheric Sciences, Fudan University, Shanghai* 200433*, China*

[4]*Function Laboratory for Ocean Dynamics and Climate, Qingdao National Laboratory for Marine Science and Technology, Qingdao* 266237*, China*

[5]*Department of Science and Technology, Parthenope University of Naples, Naples,* 80143*, Italy*

(Received 21 October 2016; revised 4 January 2017; accepted 16 January 2017)

ABSTRACT

In this study, the initial perturbations that are the easiest to trigger the Kuroshio Extension (KE) transition connecting a basic weak jet state and a strong, fairly stable meandering state, are investigated using a reduced-gravity shallow water ocean model and the CNOP (Conditional Nonlinear Optimal Perturbation) approach. This kind of initial perturbation is called an optimal precursor (OPR). The spatial structures and evolutionary processes of the OPRs are analyzed in detail. The results show that most of the OPRs are in the form of negative sea surface height (SSH) anomalies mainly located in a narrow band region south of the KE jet, in basic agreement with altimetric observations. These negative SSH anomalies reduce the meridional SSH gradient within the KE, thus weakening the strength of the jet. The KE jet then becomes more convoluted, with a high-frequency and large-amplitude variability corresponding to a high eddy kinetic energy level; this gradually strengthens the KE jet through an inverse energy cascade. Eventually, the KE reaches a high-energy state characterized by two well defined and fairly stable anticyclonic meanders. Moreover, sensitivity experiments indicate that the spatial structures of the OPRs are not sensitive to the model parameters and to the optimization times used in the analysis.

Key words: Kuroshio Extension, states transition, CNOP approach, optimal precursor, ocean modeling

Citation: Zhang, X., M. Mu, Q. Wang, and S. Pierini, 2017: Optimal precursors triggering the Kuroshio Extension state transition obtained by the Conditional Nonlinear Optimal Perturbation approach. *Adv. Atmos. Sci.*, **34**(6), 685–699, doi: 10.1007/s00376-017-6263-7.

1. Introduction

The Kuroshio Extension (KE) is the inertial jet flowing eastwards in the midlatitude North Pacific after separation of the Kuroshio Current from the Japanese coast at around (35°N, 141°E). The KE is a strong inertial jet characterized by large-amplitude meanders and energetic pinch-off eddies (e.g., Mizuno and White, 1983; Qiu and Chen, 2005). In the KE region, one of the most intense air–sea heat exchanges takes place (e.g., Taguchi et al., 2009; Kwon et al., 2010). Based on satellite altimeter measurements and eddy-resolving ocean general circulation models, many studies (e.g., Qiu and Chen, 2005; Taguchi et al., 2007, 2010; Ceballos et al., 2009; Kelly et al., 2010; Qiu and Chen, 2010; Qiu et al., 2014) have clearly shown that the KE displays a low-frequency variability on the decadal time scale that connects a weak, contracted jet state and a fairly stable and elongated jet characterized by a high total kinetic energy level and by two fairly stable anticyclonic meanders; during this transition, the jet is very convoluted and variable, with a high eddy kinetic energy level.

Such a KE state transition brings significant changes in the regional sea surface temperature and upper-ocean heat content (e.g., Qiu, 2000; Qiu and Chen, 2006, 2011). Besides, the states of the KE strongly determine the regions where phytoplankton, and hence fish, are located. Thus, the KE state transition has a significant impact on local fisheries and economies (Nishikawa et al., 2011). More importantly, the decadal variability of the KE states has a significant impact on the global climate through changing the Pacific storm track and large-scale atmospheric circulation in the Northern Hemisphere (e.g., Qiu, 2000, 2002; Joyce et al., 2009; Frankignoul et al., 2011; Ma et al., 2015; O'Reilly and Czaja,

* Corresponding author: Qiang WANG
Email: wangqiang@qdio.ac.cn

2015; Yao et al., 2016). With such broad impacts, the importance of studying the decadal variability of the KE states is evident. Therefore, it is very relevant to investigate and possibly predict the decadal variability of the KE states.

A fundamental issue in this context concerns our understanding of the physical mechanisms that cause the KE decadal variability. The dynamic mechanisms causing the transition between the low and high energy states have been explored in several observational and modeling studies (e.g., Miller et al., 1998; Schneider et al., 2002; Qiu, 2003; Qiu and Chen, 2005, 2010; Nonaka et al., 2006; Pierini, 2006, 2014; Taguchi et al., 2007; Pierini et al., 2009; Sasaki et al., 2013). Qiu and Chen (2005) showed that the KE decadal variability is in close relation with the baroclinic Rossby wave field that propagates the PDO (Pacific Decadal Oscillation) and NPGO (North Pacific Gyre Oscillation) signals from the central and eastern North Pacific into the KE region. By using a reduced-gravity shallow water model, Pierini (2006) suggested that the KE decadal variability is the manifestation of a nonlinear intrinsic mode of the ocean system in the form of a relaxation oscillation, which would emerge spontaneously in a parameter range past a homoclinic bifurcation (so-called tipping point). Based on simulations with an eddy-resolving ocean general circulation model, Taguchi et al. (2007) suggested that the broad scale Rossby wave field generated by the basin-scale wind variability triggers intrinsic mode change of the KE. Pierini (2014) shared the same view, showing that the KE state transition can be triggered by the Rossby wave field mentioned above if a time-dependent North Pacific Oscillation (NPO) wind forcing component is added to his 2006 model. Besides, many researches have pointed out that mesoscale eddies play an important role in feeding the KE dynamics (e.g., Nonaka et al., 2006; Qiu and Chen, 2010; Qiu et al., 2015). These studies provide a coherent picture of the complex interplay between intrinsic oceanic mechanisms and the effect of basin-scale wind variability: the KE decadal variability is likely to be the manifestation of a nonlinear intrinsic ocean mode excited by the arrival of sea surface height (SSH) anomalies carried into the KE region by a baroclinic Rossby wave field remotely generated by the PDO–NPGO fluctuations.

Since the KE decadal variability is basically due to complex nonlinear processes of the ocean, the prediction of the KE decadal variability constitutes a highly intricate and peculiar problem, which has attracted the attention of many researchers. By examining the lagged regression between the SSH anomalies in the KE region and those in the central and eastern North Pacific Ocean, Qiu et al. (2014) demonstrated that the KE state could be predicted at lead times of up to about six years. Through multiple simulations with an eddy-resolving ocean general circulation model driven by the observed interannually varying atmospheric forcing under slightly different ocean initial conditions, Nonaka et al. (2016) demonstrated that the potential predictability of the KE decadal variability is, to a large extent, limited by the intrinsic nature of the variability, whose magnitude is comparable to that of the deterministic wind-driven variability. Other predictability studies, based on the model of Pierini (2006), are those of Pierini et al. (2009, see section 4 therein) and of Kramer et al. (2012).

In addition, in predictability studies it is important to explore the initial perturbation that most easily results in the occurrence of some weather or climate event [this kind of initial perturbation is called an optimal precursor (OPR)]. Because the ocean initial condition has very important impacts on the prediction of the KE decadal variability, it is natural to search for the ocean perturbation that most easily results in the occurrence of the KE state transition. On the one hand, studying the OPR may improve our understanding of the dynamical processes of the KE state transition. On the other hand, intensive observations implemented over the sensitive areas defined by the spatial structures of the OPR could contribute to constructing an observation network for the KE. Such intensive observations may capture the ocean perturbations that most easily trigger the KE state transition, thus further increasing our ability to forecast the KE state transition.

By using different approaches [e.g., the Linear Singular Vectors approach and the Conditional Nonlinear Optimal Perturbation approach (CNOP)], many researchers have explored the OPRs of El Niño events (Xue et al., 1994; Duan et al., 2004), atmospheric blocking (Jiang and Wang, 2010), the North Atlantic Oscillation (Jiang et al., 2013) and the Kuroshio large meander (Fujii et al., 2008; Wang et al., 2013). Compared with other methods, the CNOP approach has been proven to be an effective way to capture the OPRs of nonlinear phenomena. As nonlinear processes play an important role in the KE variability, it is suitable to employ the CNOP approach to investigate the OPR that triggers the KE state transition.

In this context, in this paper we analyze the predictability of the transition connecting the weak and strong KE energy states by determining and analyzing the OPRs triggering such transition in the shallow water ocean model of Pierini (2006); the OPRs will be determined by means of the CNOP approach. The article is organized as follows. The shallow water ocean model, a precise definition of the basic state from which the transitions under investigation arise, the CNOP approach, and the optimization problems related to the OPR, are presented in section 2. The main results are presented and discussed in section 3; the spatial structures and evolution of the OPRs and their impact on the KE will be considered in detail. In section 4, two sets of sensitivity numerical experiments are presented. Finally, in section 5 conclusions are drawn.

2. Methodology

This section introduces the reduced-gravity shallow water model, the definition of the basic state, the CNOP approach, and the optimization problems related to the OPR.

2.1. *The shallow water model*

In this study, the reduced-gravity shallow water model by Pierini (2006) is used to investigate the OPR that triggers the

KE state transition. Despite the relatively idealized settings, the model does reproduce the essential features of the KE and its decadal variability, thanks to the presence of the most essential elements of the geometry, stratification and forcing. The model is described by a geophysical fluid system containing a thin upper active layer and a much deeper quiescent lower layer. The model is solved numerically on a Cartesian grid with spatial grid steps $\Delta x = \Delta y = 20$ km, and the temporal grid step $\Delta t_{\text{step}} = 20$ min. To simulate the KE, the model domain is set as a part of the Pacific basin (5°S–55°N, 122°E–120°W) with a schematic coastline in the western boundary, as shown in Fig. 1 [the importance of this geometric feature is discussed in Pierini (2008)]. The shallow water equations describing the flow in the upper layer are

$$\frac{\partial \boldsymbol{u}}{\partial t} + (\boldsymbol{u}\cdot\boldsymbol{\nabla})\boldsymbol{u} + f\boldsymbol{k}\times\boldsymbol{u} = -g'\nabla\tilde{\eta} + \frac{\tau}{\rho H} + A_H\boldsymbol{\nabla}^2\boldsymbol{u} - \gamma\boldsymbol{u}|\boldsymbol{u}| \,, \quad (1a)$$

$$\tilde{\eta}_t + \nabla(H\boldsymbol{u}) = 0 \,, \quad (1b)$$

where $\boldsymbol{u} = (u, v, 0)$ is the horizontal velocity vertically averaged in the upper active layer, $\boldsymbol{\nabla} = (\partial/\partial x, \partial/\partial y, 0)$, f is the Coriolis parameter ($f = 2\Omega\sin\varphi$, φ is the latitude and Ω is Earth's angular velocity), $\boldsymbol{k}$ is the unit vector in the vertical direction, g' ($= 4.41\times10^{-2}$ m s^{-2}) is the reduced gravity, $\tilde{\eta}_t$ is the interface displacement (positive downward) at time t, ρ ($= 1023.5$ kg m^{-3}) is the density of the upper layer, and $\boldsymbol{\tau}$ is the wind stress (the flow is driven by a constant-in-time climatological wind stress field, which is an analytical approximation of the climatological zonal winds; its curl is shown in Fig. 1). $H = D + \tilde{\eta}$ is the upper layer thickness, where D ($= 500$ m) is the undisturbed upper layer thickness. The SSH η (positive upward) can be obtained from $\tilde{\eta}$ through the relation $\eta \cong \tilde{\eta}\Delta\rho/\rho$. As for the dissipative terms, the model includes the lateral eddy viscosity with coefficient A_H and the quadratic interfacial friction, weighted by the coefficient γ ($= 5.0\times10^{-4}$ m^{-1}). Pierini (2006) and Pierini et al. (2009) showed that the KE variability is very sensitive to the lateral eddy viscosity coefficient. In our study, A_H is set to be $A_H \geqslant 240$ m^2 s^{-1}, which is the same value used by Pierini (2014, 2015). The motivation of this choice will be discussed in detail in the next subsection. Further details on the model implementation can be found in Pierini (2006).

2.2. *The basic state*

The transitions under investigation are now defined. As shown in Qiu and Chen (2010), in 1994 and in 2004 the KE was in a state commonly denoted as elongated Qiu (2002); this corresponds to two well defined anticyclonic meanders and to a weak variability [see Fig. 2 and Fig. 4 of Qiu and Chen (2010)]. Let us call this state StA. This condition evolved, in less than one year, towards a state (denoted here as StB) in which the meanders were much weaker and the variability was slightly higher. The yearly averaged 1995 is well representative of a StB; the yearly averaged 2005, on the other hand, receives an important contribution from the collapsing two-meander state, so it is only roughly representative of a StB.

As noted by Qiu and Chen (2010), the subsequent evolution was marked, in both cases, by the arrival of a strong negative SSH anomaly carried into the KE region by baroclinic Rossby waves (generated by PDO–NPGO fluctuation at the other side of the Pacific Ocean), as shown at $t \cong 1995.5$ yr and $t \cong 2006$ yr by the Hovmöller diagram taken along the zonal band 32°–34°N [see Fig. 6 in Qiu and Chen (2010)]. As soon as this occurred, the upstream KE path length increased and became much more variable: this condition was accompanied by a very convoluted and variable jet, as shown in the panels of years 1996 and 2006 [see Figs. 2 3 in Qiu and Chen (2010)]. We call this state StC. The further evolution led to the progressive intensification of the jet (presumably through an inverse energy cascade), which eventually attained a new StA.

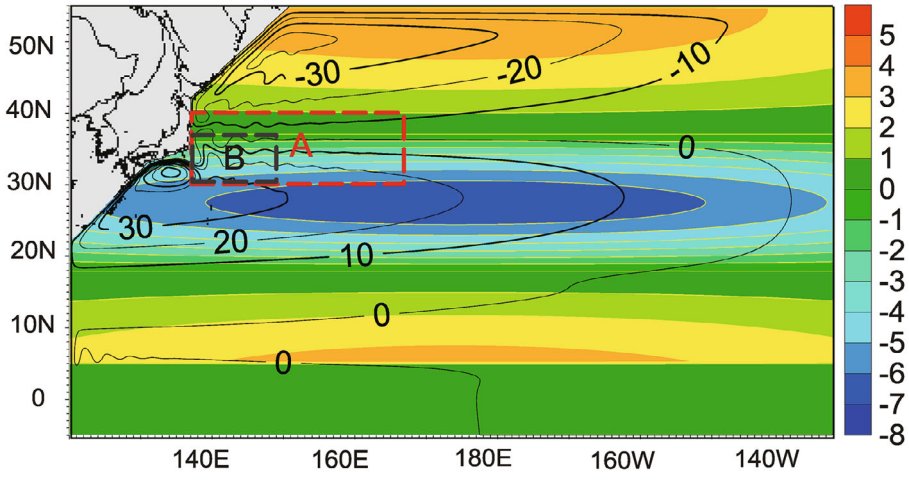

Fig. 1. Model domain (5°S–55°N, 122°E–120°W) and climatological wind stress curl (shaded; units: 10^{-8} N m^{-3}) used in the simulations. The contour lines represent the climatological mean SSH field (units: cm). The area A denotes the KE region and the area B represents the target region (see text).

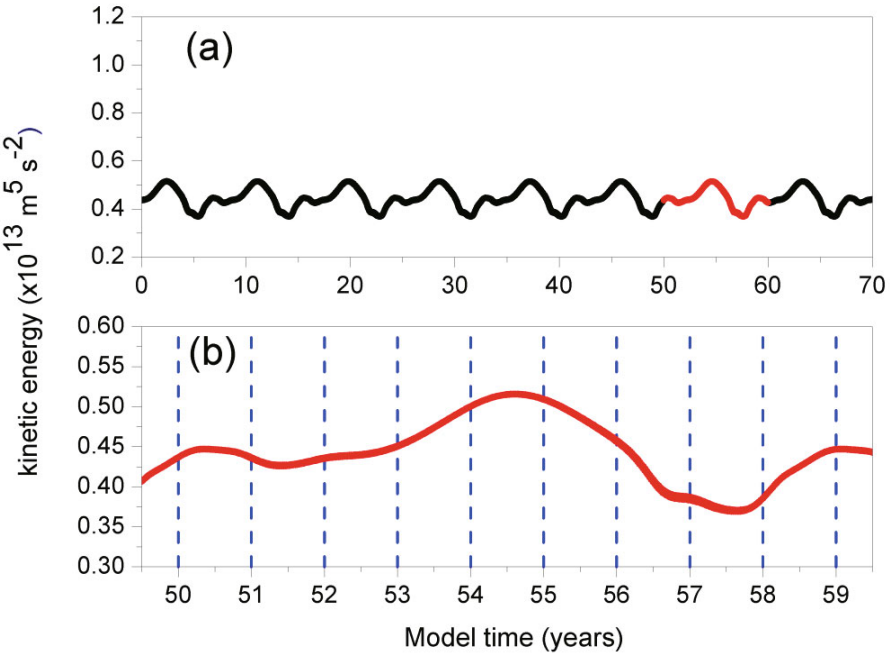

Fig. 2. (a) Time series of the kinetic energy integrated in the KE region A. The red line denotes the cycle for the calculation of the OPRs. (b) A close-up view of the time series of the kinetic energy. The blue dashed vertical lines denote the start times of the numerical experiments EXP1–10.

By using the same model described in section 2.1, Pierini (2014) found the same behavior observed through the altimeter data, provided the system is set to be excitable, e.g., if $A_H \geqslant 240$ m^2 s^{-1}. Pierini (2015) could then identify a hysteresis loop for the KE low-frequency variability in which the three states just defined were termed as persistent the meandering state (StA), stable ground state (StB), and initiation of the recharging phase (StC). In fact, in this theoretical framework, StB is stable because the system remains in a similar state until a suitable SSH anomaly excites the transition to StC (the subsequent evolution being controlled by nonlinear intrinsic oceanic mechanisms). It should be noted that, although the arrival of positive SSH anomalies in the KE region (e.g., at $t \cong 2002$ yr) were found by Qiu and Chen (2010) to correspond to the attainment of StA, those anomalies do not play an important role in the formation of such a state in the framework of our intrinsic model evolution.

The present study is aimed at analyzing the SSH anomalies that trigger the transition from StB to StC, and eventually to StA. Thus, the system must be excitable and must lie in StB, initially: this justifies the choice $A_H \geqslant 240$ m^2 s^{-1}.

2.3. *CNOP approach and optimization problems related to the OPRs*

Let us briefly recall the CNOP approach (Mu et al., 2003). The shallow water model could be formally written as

$$\boldsymbol{X}_t = M_t(\boldsymbol{X}_0)\,, \tag{2}$$

where $\boldsymbol{X}_0(= u_0, v_0, h_0)$ indicates the initial condition of the model. M_t is the nonlinear propagator that "propagates" the initial state $\boldsymbol{X}_0$ at $t = 0$ to the state $\boldsymbol{X}_t$ at the end of the optimization time Suppose the initial condition $\boldsymbol{X}_0$ is perturbed by $\boldsymbol{x}_0(= u', v', h')$: the solution can then be written as

$$\boldsymbol{X}_t + \boldsymbol{x}'_t = M_t(\boldsymbol{X}_0 + \boldsymbol{x}_0)\,, \tag{3}$$

where $\boldsymbol{x}'_t = M_t(\boldsymbol{X}_0 + \boldsymbol{x}_0) - M_t(\boldsymbol{X}_0)$ represents the nonlinear evolution of the initial perturbation $\boldsymbol{x}_0$. In order to calculate the initial perturbation that results in the maximal development at time t given the specific constraint radius δ, a nonlinear constraint optimization problem is defined as

$$J(\boldsymbol{x}_{0,\delta}) = \max_{\|x_0\|_V \leqslant \delta} J(\boldsymbol{x}_0) = \max_{\|x_0\|_V \leqslant \delta} \|M_t(\boldsymbol{X}_0 + \boldsymbol{x}_0) - M_t(\boldsymbol{X}_0)\|_B^2\,, \tag{4}$$

where $J(\boldsymbol{x}_0) = \|M_t(\boldsymbol{X}_0 + \boldsymbol{x}_0) - M_t(\boldsymbol{X}_0)\|_B^2$ is the objective function that evaluates the nonlinear evolution of the initial perturbation $\boldsymbol{x}_0$ at time t over the target region B and $\|\boldsymbol{x}_0\|_V \leqslant \delta$ is the initial constraint condition in region V with a positive constraint radius δ. If the objective function is regarded as a measure of the perturbation, the solution to the optimization problem in Eq. (4) is called the CNOP. The term "optimal" means that the value of the objective function caused by the initial perturbation is the largest for a given δ.

In this study, the unperturbed low energy state is used as the reference state, and an initial SSH perturbation $h'_{0,\delta}$ that satisfies the initial constraint condition $\|h'_0\|_V \leqslant \delta$ is superimposed on the reference state. In our reduced-gravity shallow-water model, a stream function φ can be defined from the SSH η as $\varphi = [g\rho/(f\Delta\rho)]\eta$. The velocities u and v can thus be approximated by the spatial derivatives of η (the Ekman component of the flow velocity is assumed negligible): $u = -\partial\varphi/\partial y$ and $v = -\partial\varphi/\partial x$. The velocity perturbation

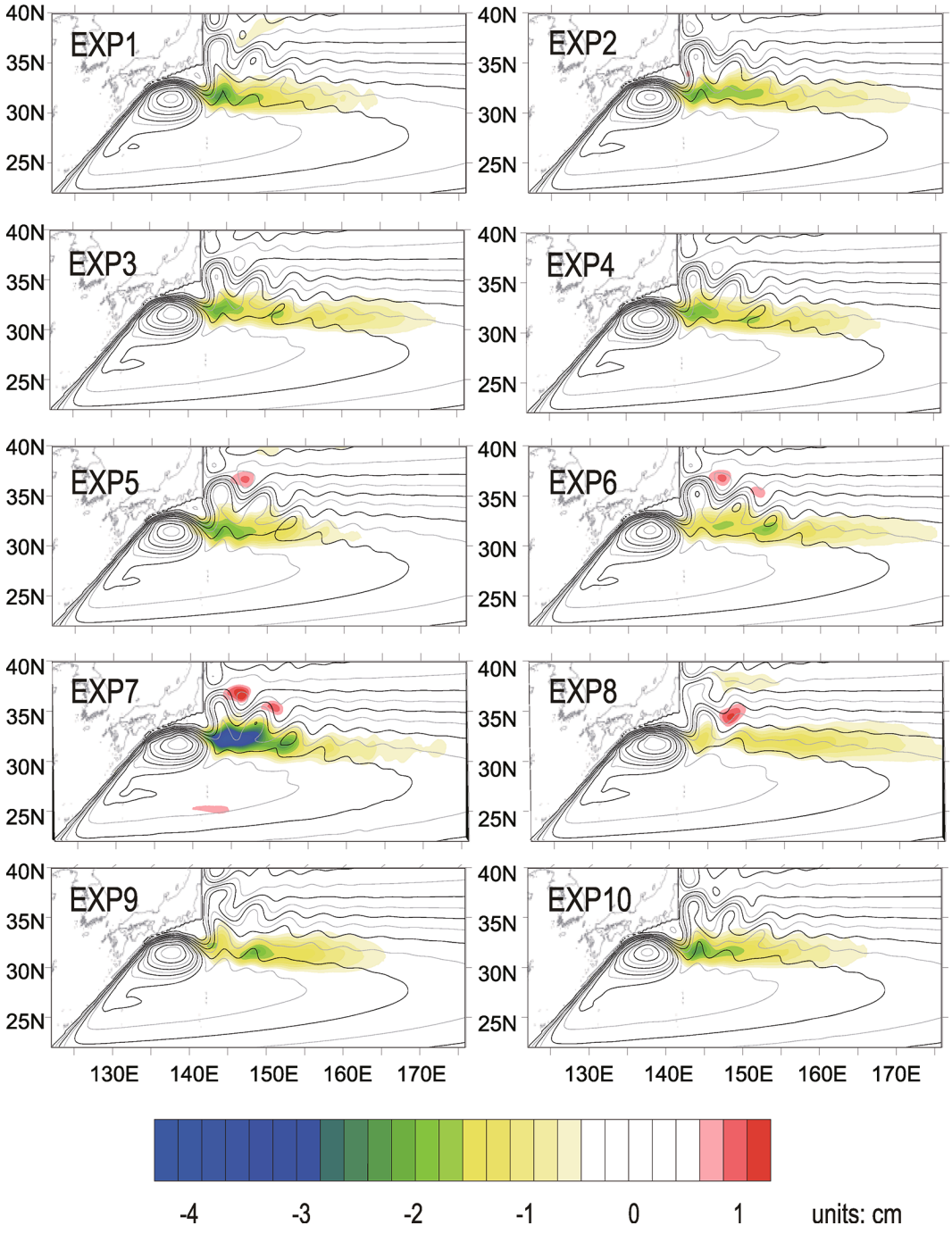

Fig. 3. SSH anomalies of the OPRs (shaded; units: cm) for the numerical experiments EXP1–10.

can then be easily obtained from the adjusted SSH perturbation. The quasigeostrophic adjustment process lasts a few hours: this short spin-up time is therefore negligible compared with the optimization time T (which is larger than one year). This justifies the perturbation of the SSH. In summary, using the CNOP approach allows one to explore what kind of initial perturbation most easily results in the occurrence of the KE state transition, which is the focus of this paper.

In general, the objective function is defined according to the specific physical problem considered. Here, the objective function is defined as the sum of the squares of the SSH perturbation over the target region B (30°–37°N, 141°–153°E, as shown in Fig. 1), so that it represents the intensity of the SSH perturbation in the KE region. Sensitivity tests suggest that using different target regions does not affect the results, as long as the target region contains the first and second anticyclonic meanders [known as the first and the second "crests", located around (35°N, 144°E) and (34°N, 151°E), respectively]. It is, in fact, in that area that the largest SSH changes occur when the KE goes through state transition. Besides, whether or not the target region contains the Kuroshio large meander (KLM) area [south of Japan, located around (32°N,

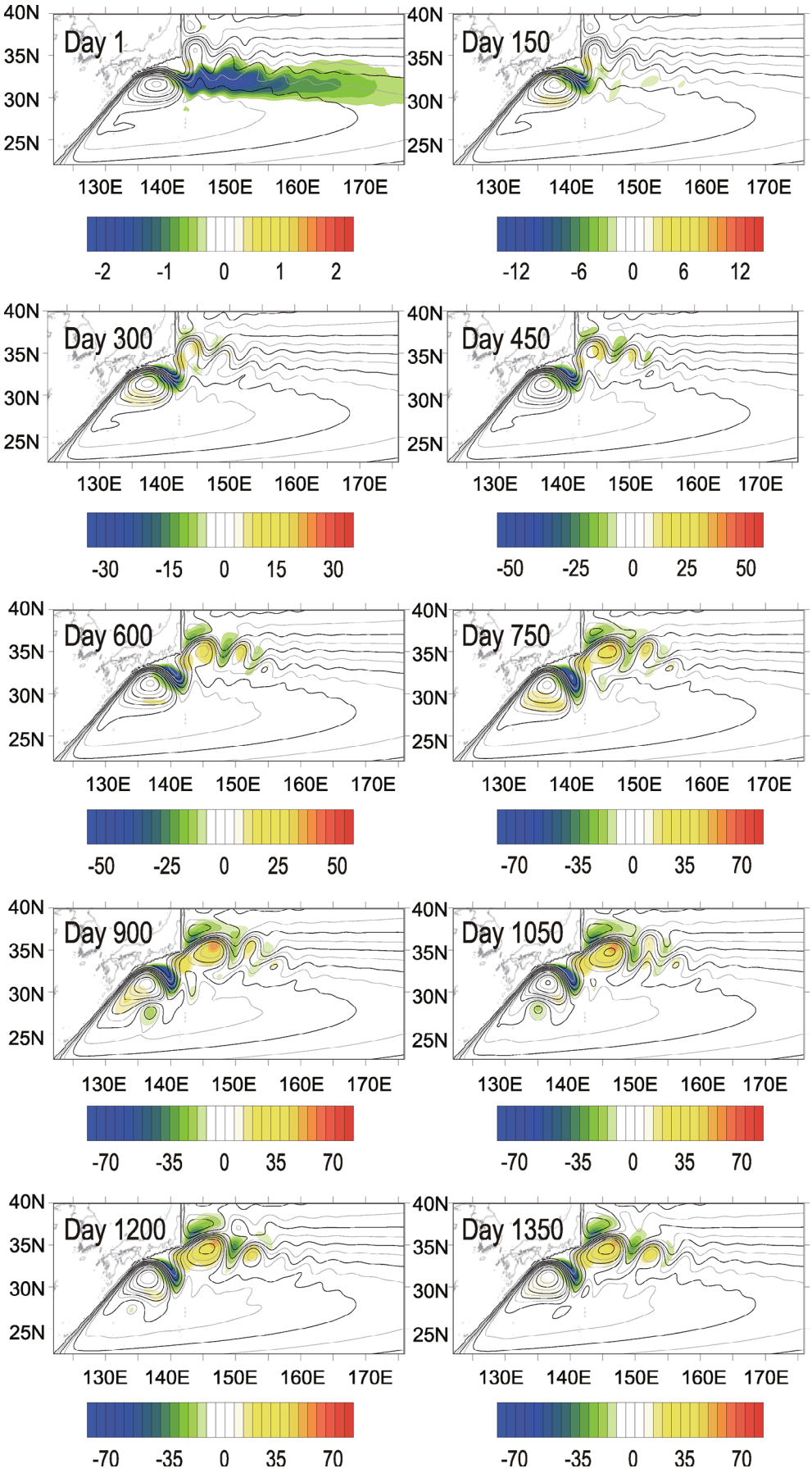

Fig. 4. SSH anomalies of the evolution of the OPR in EXP2 (shaded; units: cm).

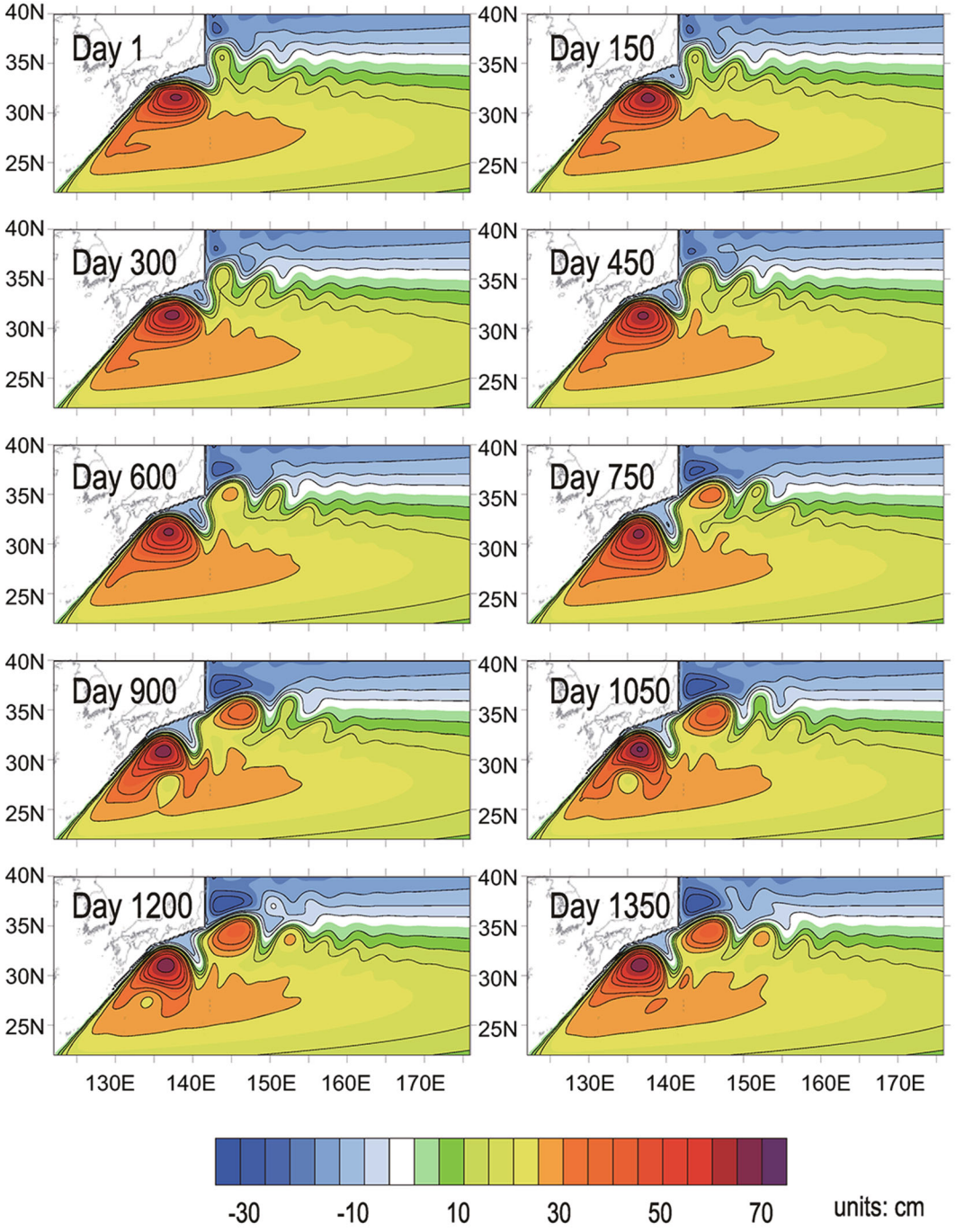

Fig. 5. Snapshots of the total SSH during the KE state transition process in EXP2 (shaded; units: cm).

140°E)], does not affect the results. However, if the objective function is estimated in the downstream region (e.g., 150°–170°E, 30°–40°N), where neither the first nor the second anticyclonic meanders are present, it will take much longer for the optimization algorithm to get the maximum value. Therefore, we chose the target region B for our objective function.

Since the KE state transition is accompanied by significant changes in the regional SSH, our choice of the objective function can be used to identify the KE state transition. Alternatively, the objective function could be chosen to represent the kinetic energy in the KE region, as Pierini (2006) did. The upstream KE path length is another efficient indicator to characterize the KE state (Qiu and Chen, 2005; Pierini, 2014).

The objective function defined here can be readily computed and the maximum can be quickly obtained by the optimization algorithm. Equation (4) can be written as

$$J(h'_{0,\delta}) = \max_{\|h'_0\|_V \leqslant \delta} J(h'_0) = \max_{\|h'_0\|_V \leqslant \delta} \int_B (h'_t)^2 dxdy\,, \qquad (5)$$

where h'_0 is the initial SSH perturbation and h'_t is the perturbed SSH at time t. $J(h'_{0,\delta})$ is the objective function, and $\|h'_0\|_V = \int_V (h'_t)^2 dxdy \leqslant \delta$ is the constraint function. We de-

fine the perturbed SSH h'_0 in the whole model domain V in order to investigate all possible initial perturbations that may trigger the KE state transition.

After setting all the optimization problems, the Spectral Projected Gradient 2 (SPG2) algorithm (Birgin et al., 2000) is used to calculate the CNOP. The SPG2 algorithm was designed to solve the minimum problem of a nonlinear function within a constraint condition δ. The problem can be formulated as

$$J(x_\delta) = \min_{x \leqslant \delta} J(x) \,, \tag{6}$$

where $J(x)$ is the objective function and $x \leqslant \delta$ indicates the constraint condition. While the SPG2 algorithm is used to compute minimization problems, the CNOP is related to the constrained maximization problems. Here, we turn the maximization problem into the minimization problem as follows:

$$J_1(h'_{0,\delta}) = -J(h'_{0,\delta}) \,. \tag{7}$$

We can then obtain the CNOP by solving the minimization problems of the objective function J_1 using the SPG2 algorithm. In the SPG2 algorithm, the gradient of the objective function with respect to the initial value is of great importance. To calculate the gradient efficiently, the tangent linear and adjoint models have been developed.

Let us rewrite the system with prognostic variables given by Eq. (3) as

$$\boldsymbol{X}_t + \boldsymbol{x}'_t = M_t(\boldsymbol{X}_0 + \boldsymbol{x}_0) = M_t(\boldsymbol{X}_0) + L_t(\boldsymbol{x}_0) + O(\boldsymbol{x}_0^2) \,, \tag{8}$$

where L_t is the tangent linear model of the original nonlinear model M_t. If the perturbation $\boldsymbol{x}_0$ is infinitesimal, the $O(\boldsymbol{x}_0^2)$ in Eq. (8) can be neglected and $\boldsymbol{x}'_t = L_t(\boldsymbol{x}_0)$ represents the linear evolution of the initial perturbation $\boldsymbol{x}_0$. Next, we consider $J(\boldsymbol{x}_0)$ in order to derive the adjoint model. It should be noted that $J(\boldsymbol{x}_0)$ is a function of $\boldsymbol{x}_0$ through the original nonlinear model M_t. The variation δJ can be expressed as

$$\delta J = \left(\frac{\partial J}{\partial \boldsymbol{x}_0}\right)^{\mathrm{T}} \delta \boldsymbol{x}_0 \,. \tag{9}$$

Since $\boldsymbol{x}'_t = L_t(\boldsymbol{x}_0)$, Eq. (9) yields

$$\frac{\partial J}{\partial \boldsymbol{x}_0} = L_t^{\mathrm{T}} \frac{\partial J}{\partial \boldsymbol{x}'_0} \,, \tag{10}$$

where the operator L_t^{T} is called the adjoint model of the original nonlinear model M_t. Once we get the adjoint model, we can easily obtain the gradient of the objective function with respect to the initial value $(\partial J)/(\partial \boldsymbol{x}_0)$ through Eq. (10). We then use the SPG2 algorithm to solve the optimization problem. More details on how the SPG2 algorithm solves the optimization problem can be found in Birgin et al. (2000) and Wang et al. (2011).

3. OPRs triggering the KE state transition

3.1. *Analysis of the OPRs*

In this section we explore the OPR triggering the KE state transition using the CNOP approach. According to previous studies (Pierini, 2006, 2014; Pierini et al., 2009), the KE oscillation produced by the model described in section 2.1 is self-sustained if A_H is smaller than the tipping point $A_H = 235$ m^2 s^{-1}. For larger values, the transition from the low to the high energy state does not emerge under the time-independent climatological wind forcing, but can be triggered by suitable time-dependent forcing, such as a red wind noise with a sufficiently large decorrelation time (Pierini, 2010) or a time-dependent NPO-like wind pattern (Pierini, 2014). In both cases the reference value $A_H = 240$ m^2 s^{-1} was chosen (see section 2.2). We, therefore, adopt the same value in the present analysis.

A 70-year-long output of the reference simulation is analyzed after spin up. Following Pierini (2006), the time series of the kinetic energy in the KE region (box A in Fig. 1) is shown in Fig. 2 to characterize the KE basic state (denoted as StB in section 2.2). This reference simulation yields a small amplitude modulation of the low energy state with a dominant period of about 10 years.

In order to obtain robust results, 10 different initial states distributed along the cycle shown in Fig. 2b are considered for the calculation of the OPRs; they are taken once a year from $t = 50$ yr (EXP1) to $t = 59$ yr (EXP10). Table 1 summarizes all the numerical experiments. The optimization time is taken as $T = 2$ yr (the sensitivity of the results to different choices of T is analyzed in section 4).

The CNOPs with different δ are computed firstly. The CNOPs that can trigger the KE transition require a sufficiently large δ, and they identify the OPRs we are looking for. The results show that the CNOP with $\delta > 3 \times 10^9$ m^4 can trigger the transition for most experiments except for EXP7, in which case $\delta > 6 \times 10^9$ m^4 is required. This implies that the strength of the OPR is related to the initial KE state. Stronger perturbations are needed to trigger the transition if the KE is shifting towards the lowest energy state. Figure 3 shows the OPRs for the 10 experiments. The perturbations lie mainly in a narrow band region (30°–33°N,

Table 1. Settings of the numerical experiments for EXP1–EXP10, SE1 and SE2.

Experiment	Start time (year)	T (years)	T_H (m^2 s^{-1})
EXP1	50	2	240
EXP2	51	2	240
EXP3	52	2	240
EXP4	53	2	240
EXP5	54	2	240
EXP6	55	2	240
EXP7	56	2	240
EXP8	57	2	240
EXP9	58	2	240
EXP10	59	2	240
SE1-260	51	2	260
SE1-280	51	2	280
SE1-300	51	2	300
SE2-1.0	51	1	240
SE2-1.5	51	1.5	240
SE2-2.5	51	2.5	240

141°–170°E) and small differences exist in their spatial structures. In particular, for most experiments except for EXP8, large amplitudes are found upstream, south of the southern recirculation gyre (SRG; 30°–33°N, 141°–153°E), while weak perturbations are located at the downstream SRG region (30°–33°N, 153°–175°E). For EXP8, the perturbations are evenly distributed in a narrow region (30°–33°N, 141°–175°E). It is worth noting that most perturbations are negative SSH anomalies. In EXP5–EXP8, weak positive SSH anomalies appear to the northern part of the KE jet (35°–37°N, 145°–150°E). Because the climatological SSH in the SRG region is higher than that in the northern part of the KE jet, all of the OPRs in the 10 experiments tend to weaken the strength of the SRG, and reduce the SSH gradient across the KE jet.

3.2. *Analysis of the growth processes*

In order to investigate the growth process of the OPRs and their effects on the KE StB, the model is integrated starting from the 10 initial states of EXP1–10, with the respective OPRs superimposed at the initial times. The SSH anomaly thus obtained for EXP2 is shown in Fig. 4 for ten consecutive snapshots, while the total SSH for the same experiment is shown in Fig. 5 (the other numerical experiments show similar evolutions).

At day 1, the perturbations mainly lie in the band (30°–33°N, 141°–170°E), with largest negative amplitudes located upstream of the KE region (141°–153°E). As the negative SSH perturbations are carried upstream by Rossby waves, they eventually locate in the KLM region. Positive SSH anomalies are located in the first crest from $t = 450$ d onwards, forming a dipole anomaly that gradually intensifies. Slighter positive SSH anomalies can be found in the second crest. These positive SSH anomalies reinforce the SSH gradient across the jet, thus increasing the KE strength. The positive perturbations in the first and the second crests intensify steadily, leading to a maximum value of ~40 cm at $t = 600$ d. Eventually, the KE shifts to the high-energy state at $t = 900$ d. From now on, the KE is characterized by two stable crests, a strong SRG, an intense meridional SSH gradient, and a larger eastward surface transport (Fig. 5).

To further explore how the OPR triggers the KE state transition, Fig. 6a shows the evolution of the upstream KE path length L_{KE} [evaluated between 141°E and 153°E, following Qiu and Chen (2005, 2010) and Pierini (2006, 2014, 2015)], along with the KE strength index [representing the averaged SSH in the region (31°–36°N, 140°–165°E), according to Qiu et al. (2014) and Pierini (2015)], for both EXP2 and the reference simulation. Meanwhile, the KE paths [defined by the 15-cm SSH contours, following Pierini (2006, 2015)] at $t = 51.0$ yr, $t = 52.0$ yr, $t = 53.0$ yr, $t = 54.0$ yr and $t = 55.0$ yr are plotted in Fig. 6b, to show the migration process of the KE path in EXP2. Besides, the time series of the kinetic energy integrated in the KE region A, for both EXP2 and the reference simulation, are shown in Fig. 7.

Figure 6a shows that the KE strength for EXP2 (blue solid line) is slightly smaller than that of the reference simulation at the initial time, because negative SSH anomalies (OPRs) are superimposed on the KE region and thus reduce the SSH. Shortly after, the KE state transition starts ($t \cong 51.5$ yr). The substantial intensification of the KE in EXP2 is accompanied by a strong variability of the KE jet, evidenced by the large amplitude oscillations of L_{KE} (red solid line) and thus associated with high eddy kinetic energy levels in the KE region (this state was termed as StC in section 2.2). This apparently counterintuitive behavior, for which the eddy activity is stronger during the strengthening of the mean jet, has been suggested to be due to an inverse energy cascade (e.g., Qiu and Chen, 2005; Qiu et al., 2008, Taguchi et al., 2010, Pierini, 2006, Yang and Liang, 2016). Correspondingly, the positive anomalies in the first crest develop (Fig. 4) and the fully developed KE state forms (Fig. 5). After $t \cong 54$ yr, both the KE strength (Fig. 6a) and the kinetic energy (Fig. 7) in the KE region stabilize to a large value and L_{KE} reduces to smaller values compared to those of the reference simulation. Accompanying this process, the KE path migrates northwards (Fig. 6b), as evidenced by the KE path in the first crest region (for instance, the position of the KE path at 143°E migrates northwards from 33°N at $t = 51$ yr to 36°N at $t = 54$ yr). In summary, the OPR triggers the KE state transition by modifying the KE frontal structure. The negative SSH anomaly of the OPR reduces the SSH gradient across the jet and weakens the KE jet strength; as a result, the KE jet becomes more convoluted with a high-frequency and large-amplitude variability accompanied by high eddy kinetic energy levels. This strengthens the jet through an inverse energy cascade which, eventually, leads to the high energy KE state.

The evolutions in the other numerical experiments are similar. For simplicity, we only display the time series of the kinetic energy in the KE region in Fig. 7. For EXP1, 3, 4, 5, 7 and 10, the evolution is basically the same as that of EXP2, described in detail above. For EXP6, the transition process is somewhat slower, as it takes one more year to complete the whole transition process. It is interesting to note that a stronger high-energy KE jet state is reached if the system is perturbed when it is in its lowest energy state, as shown by the time series of EXP8 and EXP9, which start from $t = 57$ and 58 yr, respectively. In conclusion, despite some differences in the spatial structure and evolution of the 10 experiments, the OPRs show common characteristics: negative perturbations lie mainly in a narrow band to the south of the KE jet and trigger the KE transition in about two years.

It is worth stressing that our OPRs triggering the KE transition through their negative SSH anomalies are compatible with observations. As already mentioned in section 2.2, Qiu and Chen (2005, 2010) showed that, starting from a weak jet state (denoted here as StB, e.g., as in years 1995 and 2005), the convoluted high eddy kinetic energy KE state (StC) starts when negative SSH anomalies are carried into the KE region by baroclinic Rossby waves generated to the east by PDO–NPGO fluctuations Pierini (2014) showed that the same model used in the present study is capable of reproducing such transition through the same dynamical mechanism under a suitable time-dependent forcing. Here, we have

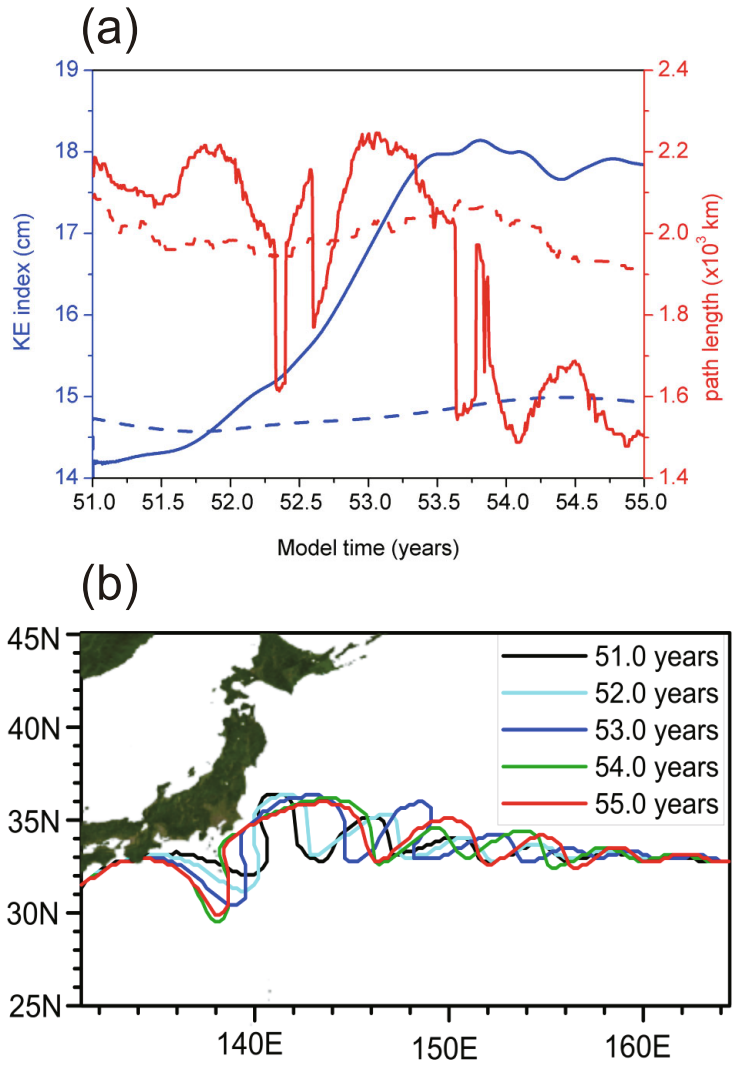

Fig. 6. (a) Time series of the KE strength index (blue lines) and KE path length (red lines) in the KE region *A* for the reference simulation (dashed lines) and for EXP2 (solid lines). (b) Paths of the Kuroshio and Kuroshio Extension defined by the 15-cm SSH contours at t = 51.0 yr, t = 52.0 yr, t = 53.0 yr, t = 54.0 yr and t = 55.0 yr.

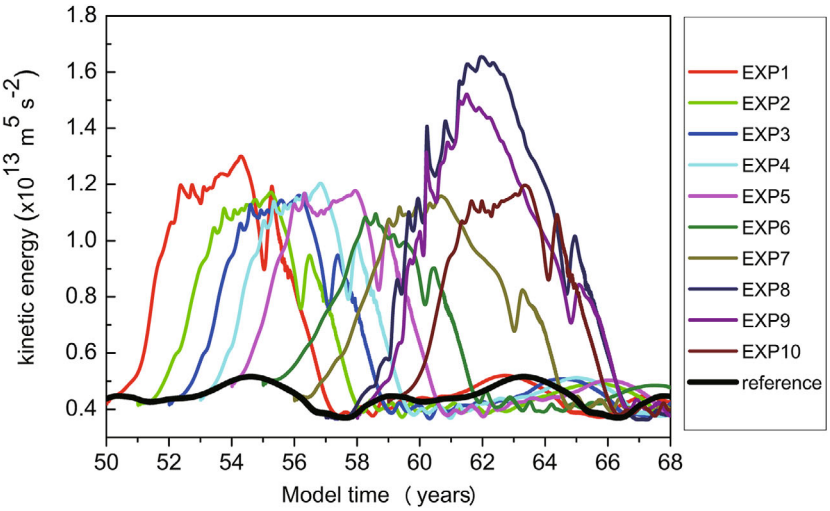

Fig. 7. Time series of the kinetic energy integrated in the KE region *A* for the numerical experiments EXP1–10 and for the reference simulation.

demonstrated that, in addition, the transition can be triggered in the model forced by the climatological time-independent forcing if a suitable negative SSH anomaly (our OPR) is superimposed on the KE ground state. The OPRs are also in substantial agreement with observations. Comparison of our OPRs (e.g., as shown in Fig. 3) with the observed anomalies [e.g, as shown in Fig. 4c of Qiu et al. (2014)] demonstrates that the former have the correct shape and are localized in the correct area, although a shift of ~1.5° to the south of the real mean latitudinal position φ (~34°N) is found (this is, however, acceptable in view of the relatively idealized nature of the model study).

This result supports the intrinsic nature of the transition. The temporal evolution of the forcing can only indirectly drive the transition. Rather, the latter is produced by dynamical mechanisms internal to the ocean system (possibly an inverse energy cascade). These mechanisms, however, need a suitable negative SSH anomaly superimposed on the KE ground state to start acting.

4. Sensitivity experiments

The results from two sets of sensitivity numerical experiments are presented in this section, with the aim to explore the sensitivity of the OPRs to the choice of the lateral eddy viscosity coefficient A_H (numerical experiments SE1) and optimization time T (numerical experiments SE2).

The appearance of the KE cycle has been shown to be very sensitive to the value of A_H, with all the other parameters held at fixed values (Pierini, 2006, 2014; Pierini et al., 2009). So, it is important to assess if the system can be excited if $A_H > 240$ m^2 s^{-1}, and how the OPRs are affected by an increased A_H. In the first set of numerical experiments (SE1), we replicate EXP2 by only changing A_H, which now ranges from $A_H = 260$ m^2 s^{-1} to $A_H = 300$ m^2 s^{-1}. For convenience, the reference experiment (EPX2, called SE1-240 here) is also presented in SE1.

Figure 8a shows the OPRs of SE1. The time series of the kinetic energy in the KE region are plotted in Fig. 8b to

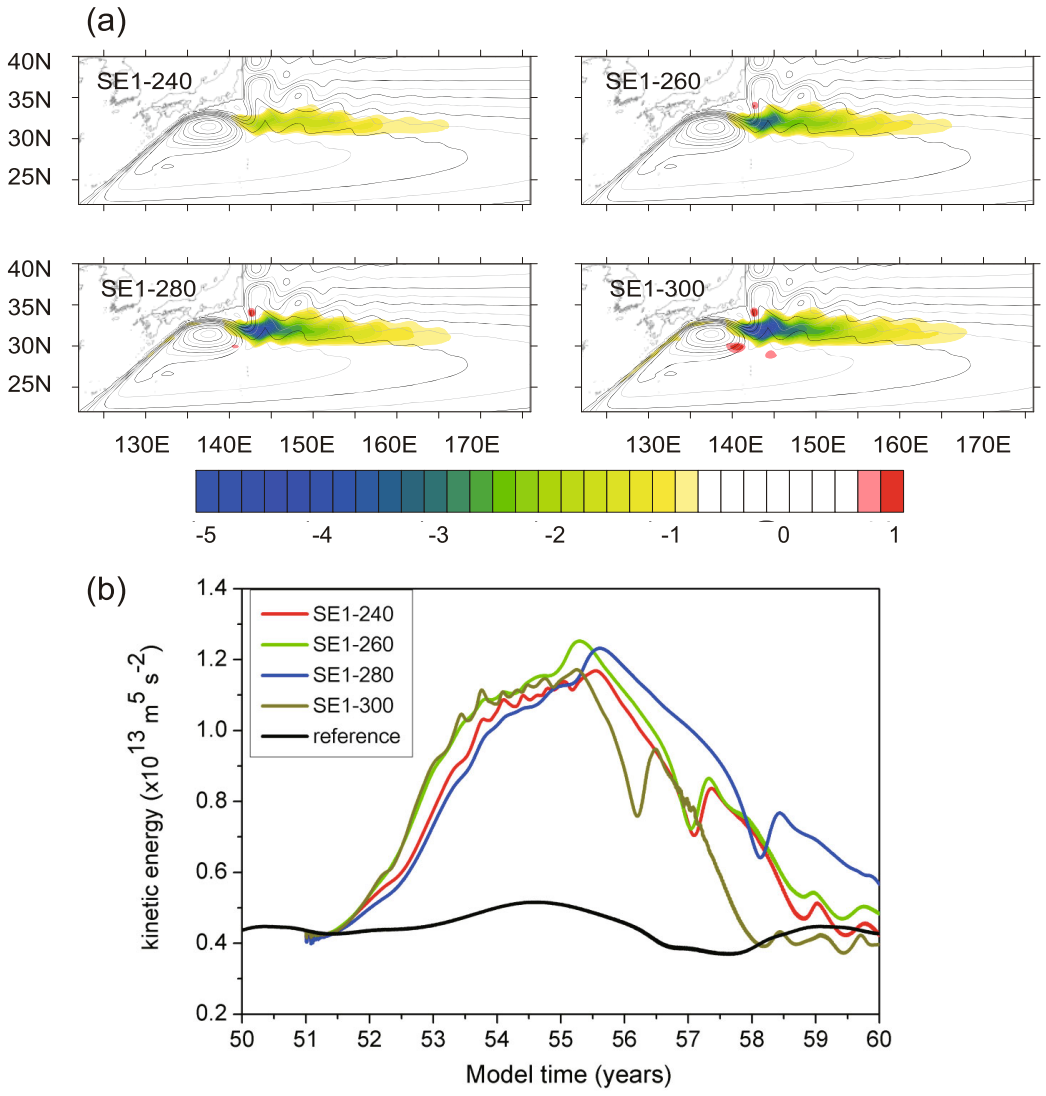

Fig. 8. (a) SSH anomalies of the OPRs (shaded; units: cm) for the set of simulations SE1. (b) Corresponding time series of the kinetic energy integrated in the KE region A.

show the KE state transition process. Clearly, the larger the A_H, the larger the OPR: when $A_H = 240$ m^2 s^{-1}, the minimum value of the OPR is −2.3 cm, while it becomes −3.4 cm when $A_H = 260$ m^2 s^{-1}, −4.2 cm when $A_H = 280$ m^2 s^{-1}, and −5.0 cm when $A_H = 300$ m^2 s^{-1}. This is because the larger the horizontal dissipation, the smaller the amplitude of the anomalies carried into the upstream KE region by the Rossby wave field, and, therefore, larger initial perturbations are needed to trigger the KE state transition.

To analyze how the spatial structures of the OPRs are modified for different values of A_H, the similarity coefficients $S_{i,j}$, defined as

$$S_{i,j} = \frac{\langle e_i, e_j \rangle}{\|e_i\| \|e_j\|}, \tag{11}$$

are used, where $\|e_i\|^2 = \langle e_i, e_i \rangle$, $i = 1, 2$ and the Euclidean inner product is computed over the whole model domain. e_1 represents the OPR of SE1-240 (the reference experiment, EXP2) while $e_{2,3,4}$ represent the OPRs of SE1-260, SE1-280 and SE1-300, respectively. The following values are obtained: $S_{1,2} = 0.9638$, $S_{1,3} = 0.9337$, $S_{1,4} = 0.9158$. The results demonstrate that, although the strengths of the OPRs depend on A_H, the spatial structures of the OPRs are very robust to changes of A_H. In conclusion, the higher values of A_H used in these experiments not only fail to prevent the typical KE cycle from emerging, they do not even modify its character. However, of course, more energetic OPRs are needed to excite the transition for values of A_H greater than that of the reference experiment.

Finally, in order to examine whether the OPRs are sensitive to the optimization time T, we perform experiments SE2 in which the reference experiment is modified only for the value of T ($T = 1$ yr in SE2-1.0, $T = 1.5$ yr in SE2-1.5 and $T = 2.5$ yr in SE2-2.5). For convenience, the reference experiment (EXP2, called SE2-2.0 here) is also presented in SE2. Figure 9a shows the OPRs of the SE2 experiments. Besides, the time series of the kinetic energy in the KE region are plotted in Fig. 9b. For SE2-1.0, the OPR is mainly located in the

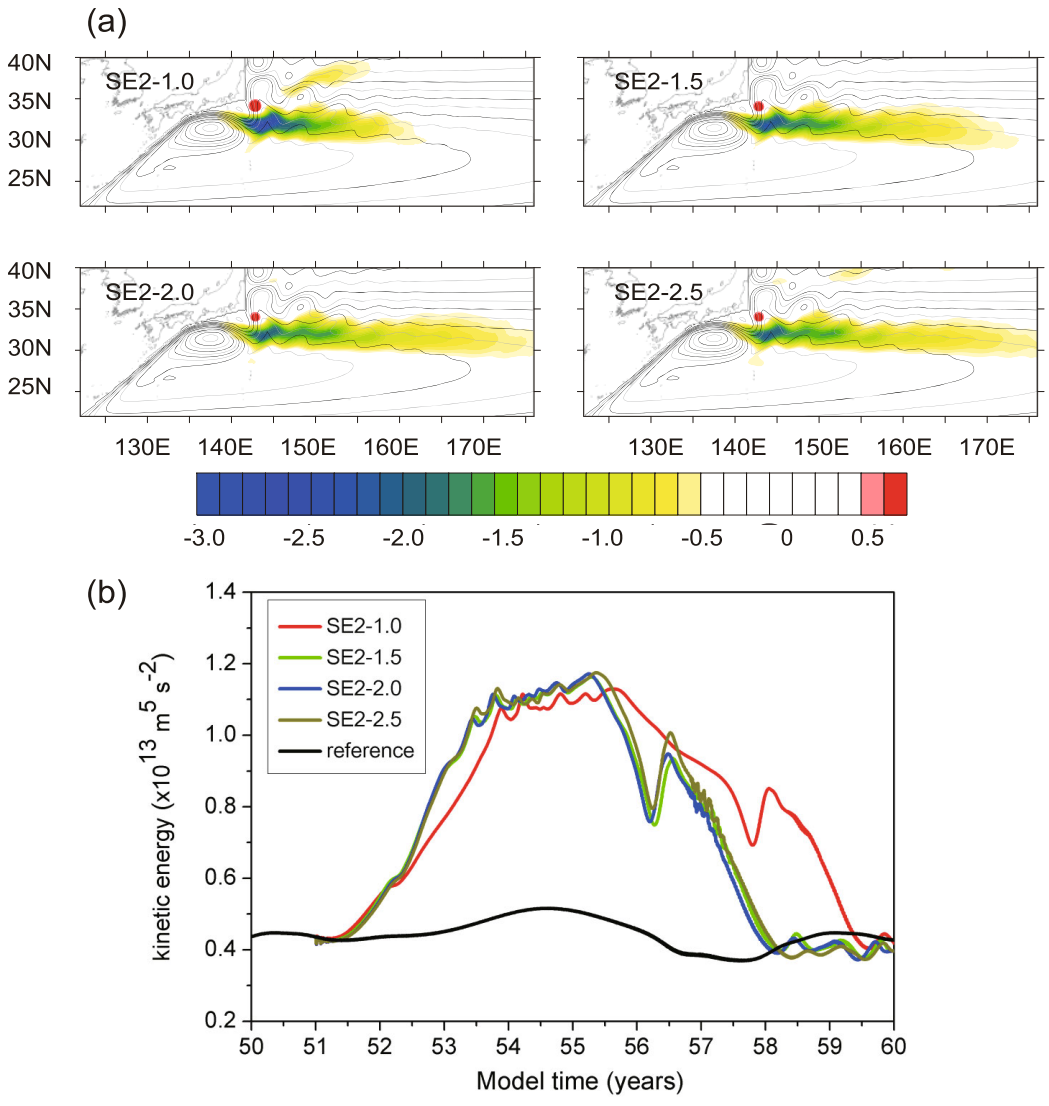

Fig. 9. (a) SSH anomalies of the OPRs (shaded; units: cm) for the set of simulations SE2. (b) Corresponding time series of the kinetic energy integrated in the KE region A.

upstream SRG region, while little perturbations are located in the downstream SRG region (the perturbations east of 160°E are very small). In contrast, the OPR in SE2-2.0 (the reference experiment, EPX2) is more evenly distributed among a narrow region around (30°–33°N, 141°–170°E) (weak perturbations can be found between 160°E and 170°E). In addition, the KE transition process in SE2-1.0 is slightly slower compared with that of SE2-2.0. Despite these subtle differences, the spatial structures and the developments of these OPRs are analogous and the coefficient $S_{i,j}$ between their spatial structures is 0.855. For SE2-1.5 and SE2-2.5 years, the spatial structures and the developments of the respective OPRs are almost the same as for SE2-2.0 (the coefficient $S_{i,j}$ between their spatial structures is 0.979 and 0.976, respectively). In summary, these sensitivity experiments prove that the qualitative conclusions regarding the changes of A_H and T, presented in section 3, are robust.

5. Conclusions

In this study, we have investigated the OPRs that induce the KE state transition from the basic ground state (StB) to the highly convoluted and variable state (StC, and, eventually, to the high energy elongated state), using a reduced-gravity shallow water ocean model and the CNOP approach. The spatial structures, growth processes and impacts of the OPRs have been analyzed in detail.

The OPRs superimposed on the basic state are found to reduce the SSH gradient across the KE jet and to weaken its strength. Initially, this triggers the transition to a convoluted jet with a strong high-frequency variability and high eddy kinetic energy levels. This in turn strengthens the KE jet through an inverse energy cascade. Eventually, the KE reaches the high energy state.

Here, we have demonstrated that the transition can be triggered in the model forced by the climatological time-independent forcing if suitable SSH anomalies (our OPRs) superimposed on the KE ground state perturb the system. The OPRs are found to be in substantial agreement with altimetric observations, being mainly located in a narrow band to the south of the KE jet. In the real ocean, similar SSH anomalies are carried into the KE region by Rossby waves generated in the eastern and central North Pacific by PDO–NPGO wind-driven fluctuations. On the other hand, their effect on the KE transition is well represented by our model excited by our OPRs. This supports the intrinsic nature of the transition.

The robustness of the OPRs has been examined by varying the time of application of the OPRs, the lateral eddy viscosity coefficient A_H, and the optimization time T. The results demonstrate that the spatial structures of the OPRs and their evolution are weakly sensitive to those changes.

It is interesting to note that the evolution of the anomalies in the first crest region of the KE is related to the evolution of the anomalies in the KLM region in the model results. This phenomenon is caused by the model features rather than the CNOP approach. In fact, Pierini (2006) mentioned this phenomenon and suggested that a possible connection between the dynamics in the Kuroshio region and that in the KLM region might exist. Interestingly, studies based on observational data (e.g., Sugimoto and Hanawa, 2012; Usui et al., 2013; Sasaki et al., 2014; Seo et al., 2014) have also revealed that the variations of the KE are interrelated to the changes of the KLM region over the long term. Understanding the dynamic mechanism that produces this relationship is beyond the scope of this paper, but this is an interesting aspect that should be analyzed in detail in future studies.

Qiu et al. (2014) demonstrated that the baroclinic Rossby wave field that propagates the SSH anomalies from the central and eastern North Pacific play a crucial role in the long-term (about six years) predictability of the KE state transition processes. However, this long-term predictive skill depends on the amplitude of the initial SSH anomalies existing in the central and eastern North Pacific Ocean and may have a lowered skill when the initial amplitude is small (e.g. the prediction started in 1997, see their Fig. 8). Besides, Nonaka et al. (2016) showed that the initial errors in the local KE region also considerably affect the predictability of the KE decadal variability. Therefore, a near-term (about two years) predictability of the KE state transition process, considering both the PDO–NPGO effects and the initial errors in the local KE region, can be expected. The OPRs obtained in this study can contribute to constructing an observational network for the KE and to applying adaptive observations in the sensitive area identified by the OPRs. These adaptive observations may capture the ocean perturbations that most easily trigger the KE state transition, meaning the near-term forecasting skill of the KE state transition process could be improved.

The results in this study were obtained by using a reduced-gravity shallow water model which, therefore, does not include baroclinic instability processes. Although Pierini (2006) showed that barotropic instability can be very effective in producing the observed transitions, baroclinic instability must clearly be taken into account in order to obtain more realistic results. To better estimate the effects of the initial errors on the prediction of the KE state transition, a more realistic and comprehensive ocean general circulation model will be used in the near future to explore the predictability of the KE state transition.

Acknowledgements. This study was supported by the National Natural Science Foundation of China (Grant Nos. 41576015, 41306023, 41490644 and 41490640), the Natural Science Foundation Of China (NSFC) Innovative Group (Grant No. 41421005), the NSFC–Shandong Joint Fund for Marine Science Research Centers (Grant No. U1406401). S. PIERINI acknowledges support from the University of Naples Parthenope (Grant No. DSTE315).

REFERENCES

Birgin, E. G., Martínez, J. M., Raydan, M., 2000: Nonmonotone spectral projected gradient methods on convex sets. *SIAM J. Optim.*, **10**(4), 1196–1211.

Ceballos, L. I., E. di Lorenzo, C. D. Hoyos, N. Schneider, and

B. Taguchi, 2009: North pacific gyre oscillation synchronizes climate fluctuations in the eastern and western boundary systems. *J. Climate*, **22**(19), 5163–5174.

Duan, W. S., M. Mu, and B. Wang, 2004: Conditional nonlinear optimal perturbations as the optimal precursors for El Niño–Southern Oscillation events. *J. Geophys. Res*., **109**(D23), D23105.

Frankignoul, C., N. Sennéchael, Y.-O. Kwon, and M. A. Alexander, 2011: Influence of the meridional shifts of the Kuroshio and the Oyashio extensions on the atmospheric circulation. *J. Climate*, **24**(3), 762–777.

Fujii, Y., H. Tsujino, N. Usui, H. Nakano, and M. Kamachi, 2008: Application of singular vector analysis to the Kuroshio large meander. *J. Geophys. Res*, **113**(C7), C07026.

Jiang, Z. N., and D. H. Wang, 2010: A study on precursors to blocking anomalies in climatological flows by using conditional nonlinear optimal perturbations. *Quart. J. Roy. Meteor. Soc*., **136**(650), 1170–1180.

Jiang, Z. N., M. Mu, and D. H. Luo, 2013: A study of the North Atlantic oscillation using conditional nonlinear optimal perturbation. *J. Atmos. Sci*., **70**(3), 855–875.

Joyce, T. M., Y.-O. Kwon, and L. S. Yu, 2009: On the relationship between synoptic wintertime atmospheric variability and path shifts in the Gulf Stream and the Kuroshio extension. *J. Climate*, **22**(12), 3177–3192.

Kelly, K. A., R. J. Small, R. M. Samelson, B. Qiu, T. M. Joyce, Y.-O. Kwon, and M. F. Cronin, 2010: Western boundary currents and frontal air-sea interaction: Gulf Stream and Kuroshio Extension. *J. Climate*, **23**(21), 5644–5667.

Kramer W., H. A. Dijkstra, S. Pierini and P. J. van Leeuwen, 2012: Measuring the impact of observations on the predictability of the Kuroshio extension in a shallow-water model. *J. Phys. Oceanogr*., **42**, 3–17.

Kwon, Y.-O., M. A. Alexander, N. A. Bond, C. Frankignoul, H. Nakamura, B. Qiu, and L. A. Thompson, 2010: Role of the Gulf Stream and Kuroshio-Oyashio systems in large-scale atmosphere-ocean interaction: A review. *J. Climate*, **23**(12), 3249–3281.

Ma, J., H. M. Xu, C. M. Dong, P. F. Lin, and Y. Liu, 2015: Atmospheric responses to oceanic eddies in the Kuroshio extension region. *J. Geophys. Res*., **120**(13), 6313–6330.

Miller, A. J., D. R. Cayan, and W. B. White, 1998: A westward-intensified decadal change in the North Pacific thermocline and gyre-scale circulation. *J. Climate*, **11**(12), 3112–3127.

Mizuno, K., and W. B. White, 1983: Annual and interannual variability in the Kuroshio current system. *J. Phys. Oceanogr*., **13**(10), 1847–1867.

Mu, M., W. S. Duan, and B. Wang, 2003: Conditional nonlinear optimal perturbation and its applications. *Nonlinear Processes in Geophysics*, **10**(6), 493–501.

Nishikawa, H., I. Yasuda, and S. Itoh, 2011: Impact of winter-to-spring environmental variability along the Kuroshio jet on the recruitment of Japanese sardine (*Sardinops melanosticus*). *Fisheries Oceanography*, **20**(6), 570–582.

Nonaka, M., H. Nakamura, Y. Tanimoto, T. Kagimoto, and H. Sasaki, 2006: Decadal variability in the Kuroshio-Oyashio extension simulated in an eddy-resolving OGCM. *J. Climate*, **19**(10), 1970–1989.

Nonaka, M., Y. Sasai, H. Sasaki, B. Taguchi, and H. Nakamura, 2016: How potentially predictable are midlatitude ocean currents? *Sci. Rep.*, **6**, 20153.

O'Reilly, C. H., and A. Czaja, 2015: The response of the Pacific storm track and atmospheric circulation to Kuroshio Extension variability. *Quart. J. Roy. Meteor. Soc*., **141**(686), 52–66.

Pierini, S., 2006: A Kuroshio Extension system model study: Decadal chaotic self-sustained oscillations. *J. Phys. Oceanogr*., **36**(8), 1605–1625.

Pierini, S., 2008: On the crucial role of basin geometry in double-gyre models of the Kuroshio extension. *J. Phys. Oceanogr*., **38**(6), 1327–1333.

Pierini, S., 2010: Coherence resonance in a double-gyre model of the Kuroshio extension. *J. Phys. Oceanogr*., **40**(1), 238–248.

Pierini, S., 2014: Kuroshio Extension bimodality and the North Pacific Oscillation: A case of intrinsic variability paced by external forcing. *J. Climate*, **27**(1), 448–454.

Pierini, S., 2015: A comparative analysis of Kuroshio extension indices from a modeling perspective. *J. Climate*, **28**(14), 5873–5881.

Pierini, S., H. A. Dijkstra, and A. Riccio, 2009: A nonlinear theory of the Kuroshio Extension bimodality. *J. Phys. Oceanogr*., **39**(9), 2212–2229.

Qiu, B., 2000: Interannual variability of the Kuroshio extension system and its impact on the wintertime SST field. *J. Phys. Oceanogr*., **30**(6), 1486–1502.

Qiu, B., 2002: The Kuroshio extension system: Its large-scale variability and role in the midlatitude ocean-atmosphere interaction. *Journal of Oceanography*, **58**(1), 57–75.

Qiu, B., 2003: Kuroshio Extension variability and forcing of the Pacific decadal oscillations: Responses and potential feedback. *J. Phys. Oceanogr*., **33**(12), 2465–2482.

Qiu, B., and S. M. Chen, 2005: Variability of the Kuroshio extension jet, recirculation gyre, and mesoscale eddies on decadal time scales. *J. Phys. Oceanogr*., **35**(11), 2090–2103.

Qiu, B., and S. M. Chen, 2006: Decadal variability in the formation of the North Pacific subtropical mode water: Oceanic versus atmospheric control. *J. Phys. Oceanogr*., **36**(7), 1365–1380.

Qiu, B., S. M. Chen, P. Hacker, N. G. Hogg, S. R. Jayne, and H. Sasaki, 2008: The Kuroshio extension northern recirculation gyre: Profiling float measurements and forcing mechanism. *J. Phys. Oceanogr*., **38**(8), 1764–1779.

Qiu, B., and S. M. Chen, 2010: Eddy-mean flow interaction in the decadally modulating Kuroshio extension system. *Deep Sea Research Part II*: *Topical Studies in Oceanography*, **57**(13–14), 1098–1110.

Qiu, B., S. M. Chen, 2011: Effect of decadal Kuroshio extension jet and eddy variability on the modification of North Pacific intermediate water. *J. Phys. Oceanogr*., **41**(3), 503–515.

Qiu, B., S. M. Chen, N. Schneider, and B. Taguchi, 2014: A coupled decadal prediction of the dynamic state of the Kuroshio extension system. *J. Climate*, **27**(4), 1751–1764.

Qiu, B., S. M. Chen, L. X. Wu, and Kida, S., 2015: Wind-versus eddy-forced regional sea level trends and variability in the North Pacific Ocean. *J. Climate*, **28**(4), 1561–1577.

Sasaki, Y. N., S. Minobe, and N. Schneider, 2013: Decadal response of the Kuroshio extension jet to Rossby waves: Observation and thin-jet theory. *J. Phys. Oceanogr*., **43**(2), 442–456.

Sasaki, Y. N., S. Minobe, and Y. Miura, 2014: Decadal sea–level variability along the coast of Japan in response to ocean circulation changes. *J. Geophys. Res*., **119**(1), 266–275.

Schneider, N., A. J. Miller, and D. W. Pierce, 2002: Anatomy of North Pacific decadal variability. *J. Climate*, **15**(6), 586–605.

Seo, Y., S. Sugimoto, and K. Hanawa, 2014: Long-term variations of the Kuroshio extension path in winter: Meridional move-

ment and path state change. *J. Climate*, **27**(15), 5929–5940.

Sugimoto, S., and K. Hanawa, 2012: Relationship between the path of the Kuroshio in the south of Japan and the path of the Kuroshio extension in the east. *Journal of Oceanography*, **68**(1), 219–225.

Taguchi, B., B. Qiu, M. Nonaka, H. Sasaki, S.-P. Xie, and N. Schneider, 2010: Decadal variability of the Kuroshio extension: Mesoscale eddies and recirculations. *Ocean Dynamics*, **60**(3), 673–691.

Taguchi, B., H. Nakamura, M. Nonaka, and S.-P. Xie, 2009: Influences of the Kuroshio/Oyashio extensions on air-sea heat exchanges and storm-track activity as revealed in regional atmospheric model simulations for the 2003/04 cold season. *J. Climate*, **22**(24), 6536–6560.

Taguchi, B., S.-P. Xie, N. Schneider, M. Nonaka, H. Sasaki, and Y. Sasai, 2007: Decadal variability of the Kuroshio extension: Observations and an eddy-resolving model hindcast. *J. Climate*, **20**(11), 2357–2377.

Usui, N., H. Tsujino, H. Nakano, and S. Matsumoto, 2013: Long-term variability of the Kuroshio path south of Japan. *Journal of Oceanography*, **69**(6), 647–670.

Wang, Q., M. Mu, and H. A. Dijkstra, 2011: Application of the conditional nonlinear optimal perturbation method to the predictability study of the Kuroshio large meander. *Adv. Atmos. Sci.*, **29**(1), 118–134, doi: 10.1007/s00376-011-0199-0.

Wang, Q., M. Mu, H. A. Dijkstra, 2013: The similarity between optimal precursor and optimally growing initial error in prediction of Kuroshio large meander and its application to targeted observation. *J. Geophys. Res.*, **118**(2), 869–884.

Xue, Y., M. A. Cane, S. E. Zebiak, and M. B. Blumenthal, 1994: On the prediction of ENSO: A study with a low-order Markov model. *Tellus A*, **46**: 512–528, http://dx.doi.org/10.1034/j.1600-0870.1994.00013.x.

Yang, Y., and X. S. Liang, 2016: The instabilities and multiscale energetics underlying the mean–interannual–eddy interactions in the Kuroshio extension region. *J. Phys. Oceanogr.*, **46**(5), 1477–1494.

Yao, Y., Z. Zhong, and X.-Q. Yang, 2016: Numerical experiments of the storm track sensitivity to oceanic frontal strength within the Kuroshio/Oyashio extensions. *J. Geophys. Res.*, **121**(6), 2888–2900.